Analytical Dirac model of graphene rings, dots, and antidots in magnetic fields

M. R. Thomsen and T. G. Pedersen
Department of Physics and Nanotechnology, Aalborg University, DK-9220 Aalborg Øst, Denmark
and Center for Nanostructured Graphene (CNG), DK-9220 Aalborg Øst, Denmark
(Received 20 February 2017; revised manuscript received 8 May 2017; published 20 June 2017)

Circularly symmetric graphene nanostructures exist in the form of graphene rings, dots, and antidots. For realistic structure sizes, atomistic studies typically become prohibitively demanding. Analytical results, however, can be found within the Dirac-equation approach even in the presence of a perpendicular magnetic field. We model nanostructure confinement by using a circularly symmetric mass term and analyze the influence of geometry, magnetic field, and mass term on the eigenstates. Excellent agreement with atomistic models for small structures is demonstrated. In addition, we find good agreement with recent magneto-transport measurements for large graphene rings and investigate their valley-dependent density of states.

DOI: 10.1103/PhysRevB.95.235427

I. INTRODUCTION

Graphene is a two-dimensional material consisting of carbon atoms in a honeycomb lattice, which has been the subject of intense research for more than a decade in part due to its remarkable electronic properties [1,2]. It is a semimetal characterized by a linear band structure near the Fermi level. The properties of graphene can be modified greatly by nanostructuring, for instance, by making graphene nanoribbons [3–5], graphene quantum dots [6,7], graphene nanorings [8–10], or periodic perforations in the graphene sheet, known as graphene antidot lattices (GALs) [11–14]. Experimentally, these structures can be made with, e.g., e-beam lithography with feature sizes down to a few nanometers [6,14–16].

Due to the linear dispersion, electrons in graphene behave as massless Dirac fermions and are to a good approximation described by the Dirac equation [2]. In this approach, confinement of electrons can be taken into account by including a piecewise constant mass term [17]. This allows for accurate modeling of the properties of nanostructured graphene structures within the Dirac approximation [18,19]. The primary advantage of using the Dirac equation is that atomistic details are ignored, making the method much faster than atomistic methods such as tight binding and density functional theory, in particular, for calculating the properties of large structures. In addition, so-called "gapped graphene" can be modeled by adding a homogeneous mass term equal to half the band gap to the Dirac Hamiltonian [20,21]. A homogeneous mass term therefore simplifies the problem further by ignoring nanostructuring as well as atomistic details. Hence, while this is accurate for the magneto-optical response of homogeneous gapped graphene [20] it fails to describe, e.g., the Hofstadter energy spectrum of graphene antidot lattices in a perpendicular magnetic field [21]. In the present work, a spatially varying mass term is applied in order to accurately describe nanostructuring.

Previous theoretical studies of nanostructured graphene in magnetic fields based on the Dirac Hamiltonian have focused on graphene antidots [22], graphene quantum dots [23–25], infinitely thin graphene rings [26], or graphene rings in a radially decaying magnetic field [27,28]. A realistic model of a graphene ring, however, must account for structures having quite dissimilar inner and outer radii, as well as the presence of constant magnetic fields. Moreover, such a model will contain the dot and antidot structures as special limiting cases. Hence, in this study, we derive the eigenvalue condition for a general graphene ring with any inner and outer radii under a constant perpendicular magnetic field. In contrast to tight-binding models, our results are fully analytical and applicable to arbitrarily large structures. We also explicitly take the limits of vanishing inner radius, giving rise to a graphene quantum dot, and outer radius approaching infinity giving rise to a graphene antidot. We show that these limits are in agreement with previous models. Furthermore, the model is compared with recent magneto-transport measurements on large graphene rings reported in Ref. [10]. Good agreement between theory and measurements is demonstrated for these structures and, moreover, we highlight their potential for valleytronics applications by studying the valley-resolved local density of states in the experimental magnetic-field range.

II. THEORY AND METHODS

We consider a graphene ring with inner and outer radii R_1 and R_2 subjected to a perpendicular magnetic field; see Fig. 1. In this manner, dot and antidot geometries are special cases of the ring; namely, $R_1 \to 0$ and $R_2 \to \infty$, respectively. The Dirac model of graphene is employed by taking the confinement into account via a piecewise constant mass term $\Delta(r)$, which is vanishing in the graphene region and equal to Δ elsewhere. Such a piecewise constant mass term reproduces the features of nanostructures confined by armchair edges, whereas edges with extended zigzag segments are more problematic, partly due to the presence of edge states [18,19,29]. The antidot [22] and dot [24,25] geometries have already been considered within this model and many steps of the current derivation are similar to those cases. Also, infinitely thin rings were previously considered within a similar model, showing very good agreement with tight-binding simulations of thin graphene rings with armchair edges [26]. Additionally, the ring geometry was considered for a radially decaying magnetic field [27,28].

Here, the general problem of a graphene ring with arbitrary inner and outer radii under a magnetic field will be considered. Experimentally, graphene nanostructures are typically etched out of larger sheets by using lithography [6,14–16]. Such graphene nanostructures are characterized by strong

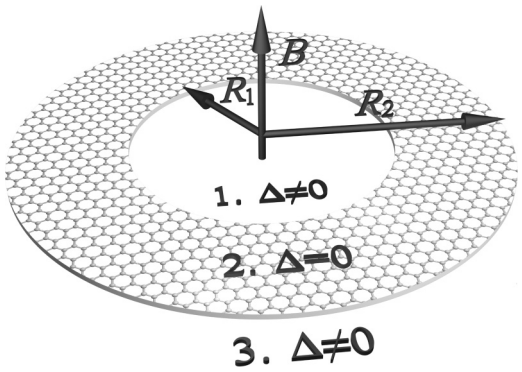

FIG. 1. Graphene ring geometry with inner and outer radii R_1 and R_2 and a perpendicular magnetic field. This system is modeled by using the Dirac equation with a spatially varying mass term, equal to Δ in regions 1 and 3 and vanishing in region 2.

confinement consistent with $\Delta \to \infty$. Alternative methods, such as hydrogenation [30] or embedding in various host materials [31], have been considered, however. In these cases, softer confinement with finite barriers can be mimicked by a finite mass term. In the present work, our primary focus will be on the $\Delta \to \infty$ limit but results valid for finite Δ are given in the appendix.

We place the graphene sheet in the (x,y) plane and take the magnetic field $\mathbf{B}$ along z. The Dirac equation reads $H\Psi = E\Psi$ with spinor wave function $\Psi = (\psi_A, \psi_B)^T$ and Hamiltonian near one of the two inequivalent Dirac valleys,

$$H = \begin{bmatrix} \Delta(r) & v_F \Pi_\mp \\ v_F \Pi_\pm & -\Delta(r) \end{bmatrix}, \tag{1}$$

where the upper (lower) sign corresponds to the K (K') valley. Here, $v_F \approx 10^6$ m/s is the Fermi velocity and $\Pi_\pm \equiv \Pi_x \pm i\Pi_y$, where $\Pi = \mathbf{p} + e\mathbf{A}$ is the generalized momentum and $\mathbf{A} = (B/2)(-y\hat{\mathbf{x}} + x\hat{\mathbf{y}})$ is the vector potential in the Landau gauge. For a region in which the mass term is constant, the eigenvalue condition for the two spinor components ψ_A and ψ_B can be decoupled, yielding

$$v_F^2 \Pi_\mp \Pi_\pm \psi_A(\mathbf{r}) = [E^2 - \Delta^2(r)]\psi_A(\mathbf{r}). \tag{2}$$

The requirement that the mass term is constant implies that this equation is valid only for $r \neq R_{1,2}$. The full solution must therefore be obtained by enforcing continuity of the wave function at the boundaries. This equation has solutions on the form $\psi_A(r,\phi) = (2\pi)^{-1/2} f(r) e^{im\phi}$, where $m = 0, \pm 1, \pm 2, \ldots$ is the angular-momentum quantum number. By introducing a dimensionless radial coordinate $\rho = r/\sqrt{2}l_B$ with magnetic length $l_B = \sqrt{\hbar/(eB)}$ and dimensionless energy $\epsilon = E/(\hbar\omega_c)$ as well as $\delta_\rho = \Delta(r)/(\hbar\omega_c)$ and $\delta = \Delta/(\hbar\omega_c)$ with cyclotron energy $\hbar\omega_c = \sqrt{2}\hbar v_F/l_B$, this leads to the eigenvalue equation

$$\left[-\frac{d^2}{d\rho^2} - \frac{1}{\rho}\frac{d}{d\rho} + \frac{m^2}{\rho^2} + \rho^2\right] f(\rho) = 2\lambda_{n,m} f(\rho), \tag{3}$$

with eigenvalue $\lambda_{n,m} = 2(\epsilon^2 - \delta_\rho^2) - (m \pm 1)$, where n is the radial quantum number. As a matter of convention, we use positive values $n = 1,2,\ldots$ for positive eigenvalue solutions and negative $n = -1, -2, \ldots$ for negative ones. It can be shown that the energy spectra of the K and K' valleys are connected through the simple operation $E_m^{(K')} = -E_{m+1}^{(K)}$, which was also noted for the antidot geometry in Ref. [22]. Note that this restores any broken electron-hole symmetry in the individual valleys. Due to this simple connection between the valleys, only one valley needs to be considered explicitly in order to construct the full energy spectrum and most of the following derivation is therefore based on the K valley.

Equation (3) has the general solution

$$f(\rho) = \rho^{-m} e^{-\frac{\rho^2}{2}} \left[\alpha L^{-m}_{\epsilon^2 - \delta_\rho^2 - \delta_K}(\rho^2) + \beta U^{1-m}_{\delta_K + \delta_\rho^2 - \epsilon^2}(\rho^2)\right], \tag{4}$$

where $U_a^b(z) \equiv U[a,b,z]$ is the confluent hypergeometric function of the second kind, $L_a^b(z)$ is the generalized Laguerre polynomial, and we have defined $\delta_K = 1$ in the K valley and $\delta_K = 0$ in the K' valley. Also, α and β are constants that must be determined from the boundary conditions. We focus on a graphene ring with inner radius $R_1 = \sqrt{2}l_B\rho_1$ and outer radius $R_2 = \sqrt{2}l_B\rho_2$ and specialize later to the cases of dots and antidots by taking the limits $R_1 \to 0$ and $R_2 \to \infty$, respectively. To satisfy normalizability of the wave function, $\beta = 0$ in region 1 and $\alpha = 0$ in region 3. The general spinors following from this procedure are given in the appendix, both in the case of finite Δ and $\Delta \to \infty$.

The primary focus here is the $\delta \to \infty$ limit of Eq. (4) because this corresponds physically to strongly confining graphene rings such as structures etched lithographically from a sheet. To this end, we apply excellent approximations of both $L^b_{-a}(z)$ and $U^b_a(z)$ that exist in the limit of large $a > 0$; namely [32],

$$L^b_{-a}(z) \simeq \frac{e^{z/2 + 2\sqrt{-az}}(-a/z)^{b/2}\cos(b\pi)}{2\sqrt{\pi}(-az)^{1/4}} \tag{5}$$

and [22,33]

$$U^b_a(z) \simeq \frac{2e^{z/2}}{\Gamma(a)}\left(\frac{z}{a}\right)^{\frac{1-b}{2}} K_{1-b}(2\sqrt{az}), \tag{6}$$

where $K_\nu(z)$ is the modified Bessel function of the second kind and $\Gamma(a)$ is the gamma function.

The eigenvalue condition is determined by requiring continuity of both spinor components at the R_1 and R_2 boundaries. In the $\Delta \to \infty$ limit, with spinor components given by Eqs. (A5) and (A6), the eigenvalue condition in the K valley becomes

$$\begin{aligned} 0 = {} & \left\{U^{-m}_{-\epsilon^2}(\rho_2^2)\left[\epsilon L^{-m-1}_{\epsilon^2}(\rho_1^2) - \rho_1 L^{-m}_{\epsilon^2-1}(\rho_1^2)\right] - \epsilon L^{-m-1}_{\epsilon^2}(\rho_2^2)\left[U^{-m}_{-\epsilon^2}(\rho_1^2) + \rho_1\epsilon U^{1-m}_{1-\epsilon^2}(\rho_1^2)\right]\right. \\ & \left. + \rho_2\epsilon U^{1-m}_{1-\epsilon^2}(\rho_2^2)\left[\rho_1 L^{-m}_{\epsilon^2-1}(\rho_1^2) - \epsilon L^{-m-1}_{\epsilon^2}(\rho_1^2)\right] - \rho_2 L^{-m}_{\epsilon^2-1}(\rho_2^2)\left[U^{-m}_{-\epsilon^2}(\rho_1^2) + \rho_1\epsilon U^{1-m}_{1-\epsilon^2}(\rho_1^2)\right]\right\} \\ & \times \left[\epsilon^2 L^{-m-1}_{\epsilon^2}(\rho_1^2) U^{1-m}_{1-\epsilon^2}(\rho_1^2) + L^{-m}_{\epsilon^2-1}(\rho_1^2) U^{-m}_{-\epsilon^2}(\rho_1^2)\right]^{-1}. \end{aligned} \tag{7}$$

The corresponding eigenvalue condition in the case of finite Δ is given in the appendix. Unless stated otherwise, eigenvalues are calculated by using the expressions for $\Delta \to \infty$.

It is interesting to note that the dimensionless lengths ρ_1 and ρ_2 are invariant to scaling simultaneously all physical lengths R_1 and R_2 by a factor a and the magnetic field B by $1/a^2$. It then follows immediately from Eq. (7) that the dimensionless energy ϵ therefore also must be invariant under this scaling and so the physical energy scales as $E \to E/a$. Therefore, by appropriately scaling the eigenvalues for a given geometry, the eigenvalues for any other system with the same R_1/R_2 ratio can be obtained. This scaling, of course, only applies whenever R_1/R_2 is finite and breaks down in the limits $R_1 \to 0$ and $R_2 \to \infty$, but is valid otherwise.

For the dot geometry, i.e., the $R_1 \to 0$ limit, the eigenvalue condition, Eq. (7), reduces to

$$\epsilon L_{\epsilon^2}^{-m-1}\left(\rho_1^2\right) + \rho_1 L_{\epsilon^2-1}^{-m}\left(\rho_1^2\right) = 0. \tag{8}$$

This expression is equivalent to the one obtained in Ref. [25] and, thus, gives rise to exactly the same eigenvalue spectrum. Also, an expression similar to this was derived in Ref. [24], but apparently their approximate expression erroneously gives the Landau levels of pristine graphene in addition to the correct spectrum (see discussion below).

Similarly, for the antidot geometry, i.e., the $R_2 \to \infty$ limit, the eigenvalue condition reduces to

$$U_{-\epsilon^2}^{-m}\left(\rho_2^2\right) + \rho_2 \epsilon U_{1-\epsilon^2}^{1-m}\left(\rho_2^2\right) = 0, \tag{9}$$

which is the same expression as derived in Ref. [22]. The fact that the ring eigenvalue condition, Eq. (7), readily reduces to the well-known expressions for dot and antidot geometries testifies to the correctness of the obtained expression. Note that these eigenvalue expressions can also be derived by using an equivalent boundary condition requiring zero outward particle current on the boundary, as discussed in the appendix.

As discussed above, the Dirac approach is an approximation to more accurate but computationally demanding atomistic methods. Hence, in order to validate the current Dirac model, we compare below to tight-binding simulations for structures sufficiently small to allow an atomistic approach. For this purpose, we use a nearest-neighbor tight-binding model with the Hamiltonian

$$\hat{H} = -t \sum_{\langle i,j \rangle} \hat{c}_i^\dagger \hat{c}_j, \tag{10}$$

where $\hat{c}_i^\dagger$ and $\hat{c}_j$ are creation and annihilation operators, respectively, $t = 3.033$ eV is the hopping parameter, and $\langle i,j \rangle$ denotes nearest neighbors. In this case, the magnetic field is incorporated via a Peierls substitution [20,21] $t \to t \exp(i\phi_{ij})$ with the Peierls phase $\phi_{ij} = e/\hbar \int_{\mathbf{r}_i}^{\mathbf{r}_j} \mathbf{A} \cdot d\mathbf{l}$ for a pair (i,j) of atoms.

III. RESULTS

The eigenvalue spectra of graphene rings, dots, and antidots for several values of n and m are shown in Fig. 2 for both K and K' valleys. Despite the geometric differences between these three systems, some similarities are observed: The magnetic-field dependence of ring and the antidot spectra

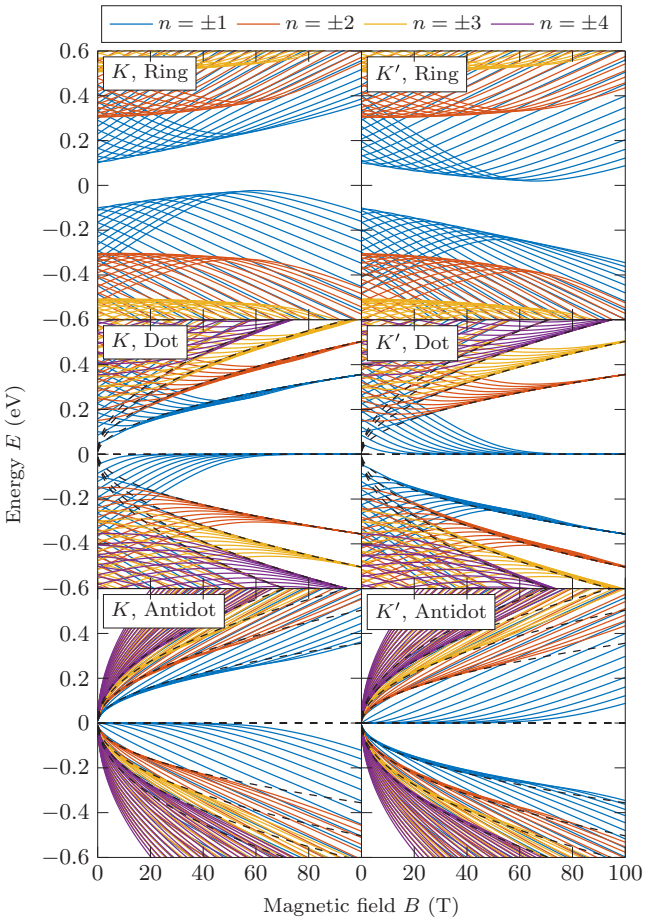

FIG. 2. Eigenvalue spectra of ring, dot, and antidot systems with inner and outer radii $R_1 = 10$ nm and $R_2 = 20$ nm in the K (left) and K' (right) valleys for $-4 \leqslant n \leqslant 4$ and $-10 \leqslant m \leqslant 10$. The dashed black lines show the Landau levels ($|n| \leqslant 4$) of pristine graphene.

are both approximately linear at large field strength, while the ring and dot spectra are nearly linear at low magnetic fields. These similarities will be discussed in more detail below.

One feature that is immediately evident is that the magnetic field lifts the valley (or pseudospin) degeneracy for all three geometries. This is especially pronounced in the ring system due to the presence of a band gap that persists even for large values of the magnetic field. The lifting of valley degeneracy in graphene systems in magnetic fields is well known and has, for instance, been reported for graphene quantum dots [25] and graphene rings in a radially decaying magnetic field [27]. This lifting of valley degeneracy could make nanostructured graphene, especially graphene rings, suitable candidates for valleytronics applications.

To illustrate the asymptotic behavior under large magnetic fields, the Landau levels of pristine graphene, $E_n = \mathrm{sgn}(n) v_F \sqrt{2e\hbar B|n|}$ are included in Fig. 2 for both dot and antidot spectra. The confinement by the outer boundary is lifted when $\rho_2 = R_2/\sqrt{2}l_B \to \infty$, i.e., either the magnetic field or the outer radius tends to infinity. In this limit, the Landau levels of pristine graphene should be recovered for the dot geometry. Indeed, it is seen that the energy spectra

of the dot converge to the pristine graphene spectrum at large magnetic fields. The convergence towards the Landau levels of pristine graphene for large magnetic fields was also noted in Ref. [24]. Similarly, the confinement by the inner boundary is lifted when $\rho_1 = R_1/\sqrt{2}l_B \to 0$, i.e., either the inner radius or the magnetic field tends to zero. In this limit, the Landau levels of pristine graphene should be recovered for the antidot geometry. At low magnetic fields, the antidot energy spectra, indeed, contain several degenerate eigenvalues, which coincide with the Landau levels of pristine graphene. In fact, as m is increased and the wave function pushed away from the antidot, the Landau levels of pristine graphene are always recovered, plus additional states for lower values of m corresponding to states localized near the antidot. In the ring system, confinement by either the inner or outer boundary is felt in both of these limits and, therefore, the spectrum never fully converges to that of pristine graphene.

The band gap of the dot system closes rather fast with increasing magnetic field to reveal the equivalent of the zeroth Landau level, the LL0 state, of pristine graphene. At large magnetic fields, this state is degenerate for all values of m. The antidot system also has states resembling the LL0 state, but these are only fully degenerate in m at vanishing magnetic field. The band gap of the ring system remains at these magnetic fields, at least for the shown values of m. This is primarily due to the additional confinement compared with both dot and antidot systems.

It was noted in Ref. [26] that states having positive energy that decreases with magnetic field are associated with clockwise bond currents in the ring. Similarly, negative energies increasing with field correspond to counterclockwise currents. This means that the magnetic field will tend to localize these currents on the inner and outer boundary for these two types of states, respectively, due to the Lorentz force [34]. This also immediately explains why the dot spectrum is dominated by energies with negative slope and why the antidot spectrum is dominated by energies with positive slope. Moreover, it lies behind the transition from negative to positive slope in the ring spectrum, as the magnetic field begins to localize electrons on the inner boundary.

The magnetic-field dependence of the eigenvalue spectra for ring, dot, and antidot geometries having inner and outer radii $R_1 = 10$ nm and $R_2 = 20$ nm, respectively, is compared in Fig. 3 for different values of m. A striking feature of this plot is that the energy spectra of the ring seem to "interpolate" between the dot and antidot cases. Hence, in low magnetic fields, the ring and dot energies are similar; in particular, for large $|m|$. Similarly, for large B the ring and antidot spectra agree. A qualitative understanding of these observations can be gained from inspection of the associated wave functions, which we display in Fig. 4 for representative magnetic fields. Hence, with increasing magnetic field, the wave function is increasingly confined to smaller radii, as seen in Fig. 4. Therefore, the wave function of the ring system is only weakly influenced by the outer boundary and the eigenvalues become similar to the eigenvalues of the corresponding antidot system. On the other hand, when the magnitude of the angular-momentum quantum number m is increased, the wave function is pushed outwards by the centrifugal effect as seen in Fig. 4 for $B = 10$ T and

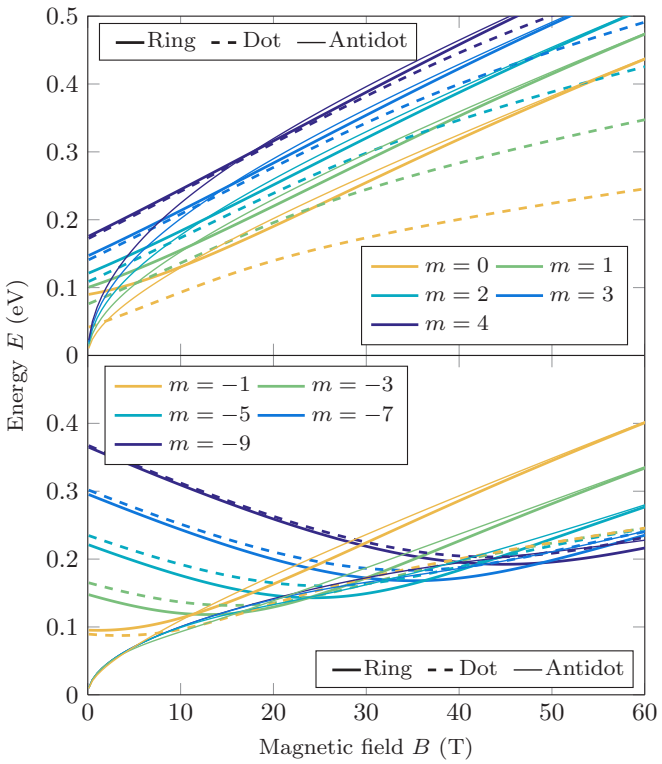

FIG. 3. First positive eigenvalue in the K valley as a function of magnetic field for ring, dot, and antidot geometries with inner and outer radii $R_1 = 10$ nm and $R_2 = 20$ nm for different values of m.

$m = 4$ or $m = -9$. Thus, as long as the magnetic field is not too large, the wave function will be only weakly influenced by the inner boundary. In this limit, the eigenvalues of the ring system will therefore be similar to the eigenvalues of the dot system. Consequently, the ring wave function is primarily confined by the inner boundary for large magnetic fields and by the outer boundary for large m. Due to this relationship, the eigenvalues of the ring system are approximately $\epsilon^{(\mathrm{ring})}_{n,m}(B) \approx \max(\epsilon^{(\mathrm{dot})}_{n,m}(B), \epsilon^{(\mathrm{ad})}_{n,m}(B))$, where $\epsilon^{(\mathrm{dot})}_{n,m}(B)$ and $\epsilon^{(\mathrm{ad})}_{n,m}(B)$ are the eigenvalues of the dot and antidot systems, respectively. Note, that it is apparent from the wave functions that the f and g spinor components are equal on the R_2 boundary for the ring and disk systems; see Fig. 4. Also, the f and g spinor component are equal but for a sign on the R_1 boundary. This is consistent with the boundary condition of no net outward particle current on the boundary as discussed in the appendix.

The similarity between the ring and dot states can be quantified by calculating the overlap integral between the ring and dot wave functions, given by $S^{(n,m)}_{\mathrm{ring,dot}} = \int (\Psi^{(n,m)}_{\mathrm{ring}})^* \Psi^{(n,m)}_{\mathrm{dot}} d^2\mathbf{r} = \int (f^{(n,m)}_{\mathrm{ring}} f^{(n,m)}_{\mathrm{dot}} + g^{(n,m)}_{\mathrm{ring}} g^{(n,m)}_{\mathrm{dot}}) r dr$. The overlap integral between the ring and antidot wave functions is calculated in the same way. The overlap integral is plotted as a function of magnetic field in Fig. 5 for different values of m. The figure shows that the overlap between the ring and antidot wave functions is essentially zero at vanishing magnetic field and converges towards unity for large magnetic fields. It is seen that the convergence is faster for numerically small values of the angular-momentum quantum number m. The reason for this

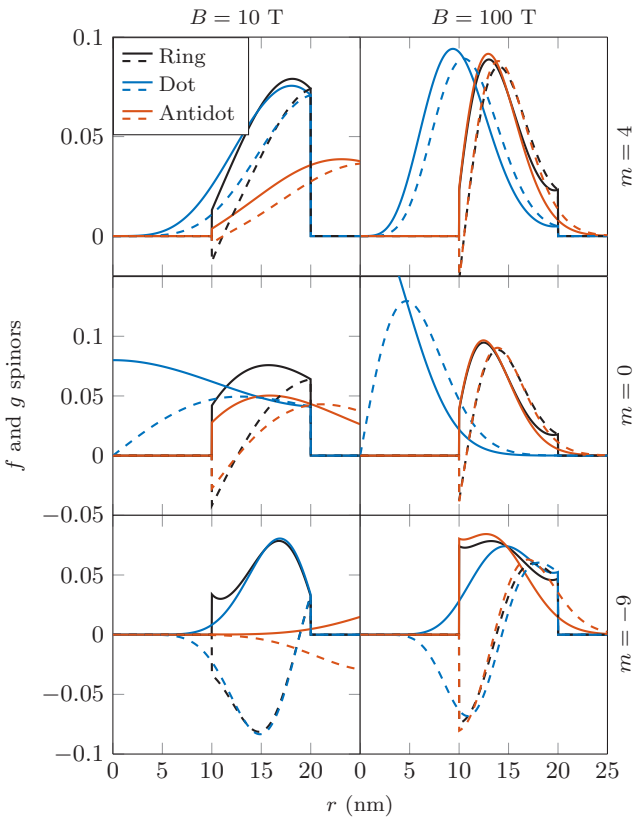

FIG. 4. Eigenstate spinors of ring, dot, and antidot systems at different values of B and m in the K valley. The solid and dashed lines are the f and g spinor components, respectively.

is that, as m increases, the wave function is pushed outward as discussed above, which increases the influence of the outer boundary. For the same reason, the overlap integral between the ring and dot wave functions is converging towards unity for

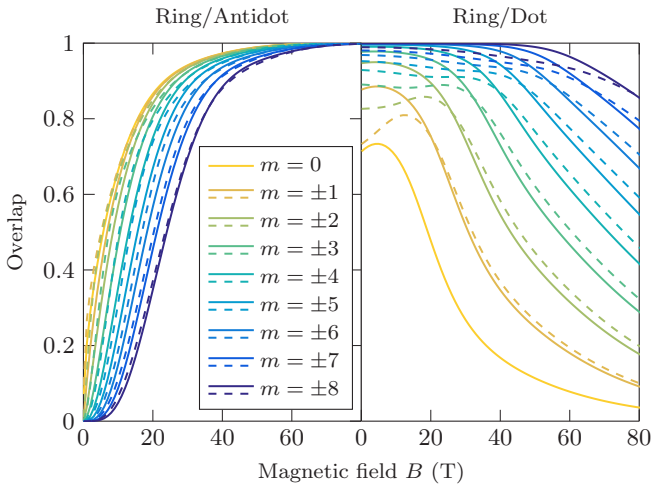

FIG. 5. Calculated overlap between the ring wave function and either the antidot (left) or dot (right) wave function as a function of magnetic field for the eigenstates of the first positive eigenvalue at different values of m in the K valley. Solid (dashed) lines are for $m \geqslant 0$ ($m < 0$).

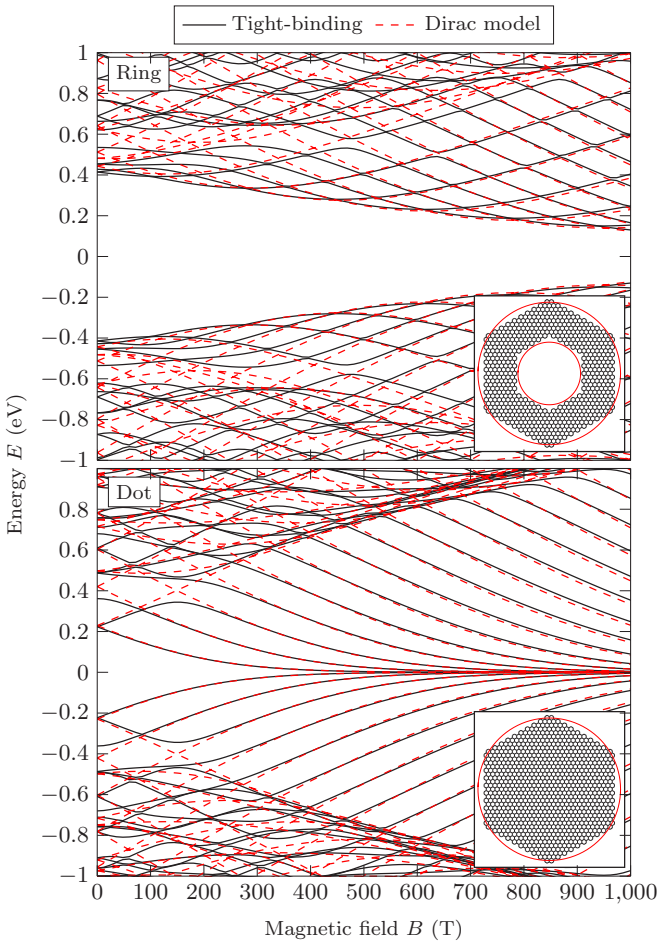

FIG. 6. Comparison between eigenvalue spectra calculated with the current Dirac model and tight-binding for ring and dot geometries. The tight-binding geometries are chosen as hexagonal with armchair edges having side lengths of the inner and outer boundaries $5\sqrt{3}a$ and $10\sqrt{3}a$, respectively, where $a = 0.246$ nm is the graphene lattice constant. The radii used in the Dirac model were chosen to fit the tight-binding geometry. The geometries used in tight-binding (black) and Dirac (red) models are shown in the insets.

numerically large values of m, while it is converging towards zero for large magnetic fields.

To validate the current model, it is compared with nearest-neighbor tight-binding simulations for similar geometries in Fig. 6 for the dot and ring. The antidot geometry is not included here, because it is not straightforward to model in tight binding, as it would essentially require an infinite number of atoms. The geometries in tight binding are chosen as hexagonal with armchair edge chirality in order to avoid edge states, which occur for extended zigzag edges [18,19,35] and which are absent in Dirac-equation-based models [18,19]. The radii used in the Dirac model were chosen to fit the tight-binding geometries, as shown in the insets of Fig. 6. The spectra show very good agreement between Dirac and tight-binding models, especially for the states closest to the Dirac point. It is not surprising that the agreement is best for these states because the Dirac model is based on a linearization of the tight-binding band structure near one of the Dirac points. In addition, excellent agreement is observed for the lowest states in high

magnetic fields. This follows from the fact that, in sufficiently high fields, the magnetic length becomes smaller than the characteristic dimension of the nanostructure. Hence, the emerging bulk-like Landau levels are less affected by the edges and very well described by the Dirac model. For instance, the magnetic length becomes less than the outer side length in Fig. 6 already at $B \approx 35$ T. We have compared the spectra for relatively small geometries due to the numerical complexity of the tight-binding calculations. However, it is worth noting that all energies approach the Dirac point when the size of the geometry increases, which should increase the agreement between tight binding and the Dirac model. In the tight-binding spectrum, some of the energy crossings observed in the Dirac spectrum are avoided. Clearly, perfect circular symmetry is broken in the atomistic model as a consequence of the hexagonal shape of the ring or dot and, also, at the level of the graphene lattice itself. This effectively leads to coupling between states, which is observed in the spectra as avoided crossings.

We noted above that an eigenvalue condition similar to ours for the dot geometry was derived in Ref. [24], leading to the same spectrum as our model but, additionally, giving the Landau levels of pristine graphene. We can substantiate our claim that these additional states should not be present by observing that these states are not present in the tight-binding model. Additionally, the pristine Landau levels are absent in other models of graphene quantum dots found in the literature [23,25]. Note also that, unlike the result obtained in Ref. [26], the result obtained here for the ring geometry does not require the ring to be particularly thin in order to give good agreement with tight binding.

To investigate the effects of softer confinement, we compare the infinite and finite Δ cases by using Eq. (A4) for varying Δ in Fig. 7. The figure shows that all eigenvalues converge to the $\Delta \to \infty$ limit as the mass term is increased. In the limit of vanishing Δ, confinement of the electrons is absent and the eigenvalues converge to the pristine Landau levels, with Landau level index $n = (m + |m|)/2 + \delta_K$, which also means that all eigenvalues are degenerate for $m \leqslant 0$. As the figure shows, the positive-m states shift towards the $\Delta \to \infty$ limit and the degenerate $m \leqslant 0$ states split when Δ is close to the energy E. This is the expected result, because the confining potential should be larger than the energy of the state in order to confine the electron. The transition is gradual for small magnetic fields and more abrupt for large fields. The transition range may be seen as a competition between the geometric confinement Δ and the characteristic magnetic energy, i.e., the cyclotron energy $\hbar\omega_c$. For $B = 10$ and $B = 100$ T fields, $\hbar\omega_c$ is approximately 114 and 362 meV, respectively. Correspondingly, the mass term must be significantly larger in the $B = 100$ T case to have any noticeable influence on the states.

The theoretical framework presented here is readily applicable to structures of experimental relevance. Because of the Dirac approximation, even very large nanostructures can be treated, in contrast to atomistic approaches. A case in point is the very recent magneto-transport measurements of Ref. [10]. There, graphene rings having inner and outer radii 200 nm and ∼400 nm, respectively, were studied in a geometry allowing for carrier doping via electrostatic gating. For slightly p-doped structures, pronounced Aharonov–Bohm-type (AB-type) oscillations were observed above a certain threshold value of the

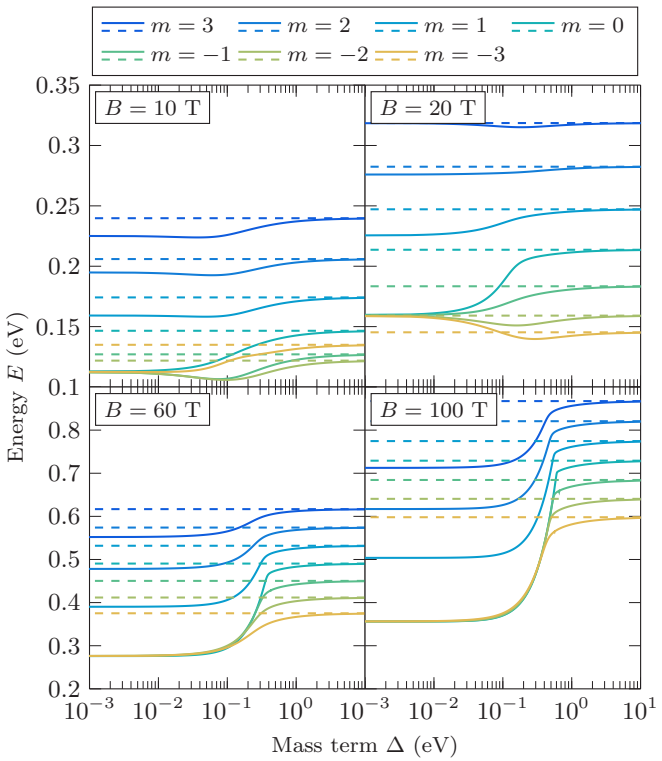

FIG. 7. First positive eigenvalue in the K valley as a function of the mass term for a graphene ring with inner and outer radii $R_1 = 10$ nm and $R_2 = 20$ nm for different values of m, calculated by using Eq. (A4). The dashed lines show the corresponding values obtained for an infinite mass term calculated by using Eq. (7).

magnetic field of about 0.1 T. In Fig. 8, we plot the energies of a graphene ring taking $R_1 = 200$ nm and $R_2 = 350$ nm. We plot only the negative eigenvalues corresponding to a p-doped sample but, naturally, the positive ones lie symmetrically above zero. The observation of a threshold magnetic field may be interpreted as follows: As illustrated in Fig. 8, the confinement-induced band gap is predicted to decrease in a magnetic field. Hence, in cases of dilute doping, the Fermi level may lie in the gap at low fields. Upon increasing the field, the Fermi level will cross the band edge, however, and this will coincide with the onset of AB oscillations. For a threshold magnetic field of 0.1 T, this line of reasoning fixes the Fermi level at approximately −4 meV as indicated by the dashed line in Fig. 8.

We may now read off the magnetic fields, at which the Fermi level coincides with one of the calculated eigenvalues. In this manner, the intersections illustrated by the vertical lines in Fig. 8 are extracted. These intersections are seen to follow a quasiperiodic pattern as expected for AB oscillations. The period of about 0.012 T corresponds reasonably well with the measured AB resonances indicated by crosses in the figure. The discrepancy between calculated and measured magnetic fields ΔB is shown in the inset and seen to be in the few-mT range. Thus, the theory is in good agreement with these measurements. We note, however, that the outer radius has been taken to be slightly less than the experimental estimate. In fact, if an outer radius of 400 nm is used, we find energy eigenvalues lying somewhat closer than the measured ones.

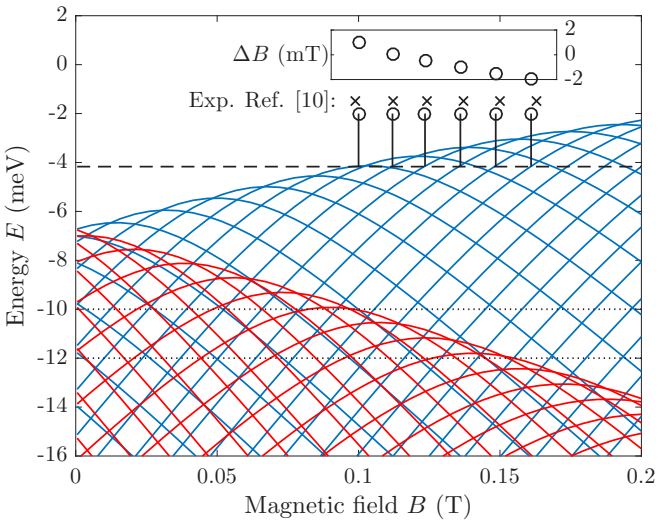

FIG. 8. Energy eigenvalues of a graphene ring with $R_1 = 200$ nm and $R_2 = 350$ nm with contributions from the K (blue) and K' valleys (red). The dashed line indicates the Fermi level determined from the band edge at $B \sim 0.1$ T. The vertical lines show the magnetic-field values, at which eigenvalues coincide with the Fermi level. Crosses are experimental Aharonov–Bohm resonances from Ref. [10] and the deviation between calculation and experiment ΔB is shown in the inset. The dotted lines define the energy range used to compute the local density of states in Fig. 9.

Whether the outer radius used in the experiment is, in fact, closer to 350 nm is unclear. It is gratifying, however, that the overall experimental features are reproduced by theory. We further note that this structure contains more that eight million atoms and would, therefore, be very difficult to handle with atomistic approaches.

To further stress the applicability of the analytical Dirac approach, we now consider the valley-resolved local density of states (LDOS) for the large ring studied in Fig. 8. The LDOS is probed in transport experiments such as tunneling spectroscopy. In practice, measurements probe a finite energy range determined by the experimental resolution and, consequently, we consider the LDOS sampled over a finite energy range. To this end, we select the range between $E_1 = -12$ meV and $E_2 = -10$ meV indicated by the dotted lines in Fig. 8 and fix the magnetic field at $B = 0.1$ and 0.15 T. This energy range is selected because the balance between K and K' contributions varies significantly in the experimental magnetic field range; c.f. Fig. 8. The LDOS is then calculated as $L(\mathbf{r}) = \sum_{E\in[E_1,E_2]} |\psi_E(\mathbf{r})|^2$ with ψ_E being a state having energy E. As clearly demonstrated in Fig. 8, this energy range contains contributions from both the K (blue) and K' (red) valleys. We compute the LDOS for each valley separately in order to distinguish between the two valley contributions. The results, shown in Fig. 9(a), illustrate this difference very clearly. Thus, the LDOS of the K valley is only about half of the K' LDOS at $B = 0.1$ T. In contrast, the two contributions are roughly equal at $B = 0.15$ T. In both cases, the LDOS tends to decrease with radial distance and with a slight oscillatory modulation superimposed on the decrease. The difference between valley contributions follows from the number of states in the energy range considered, as shown in

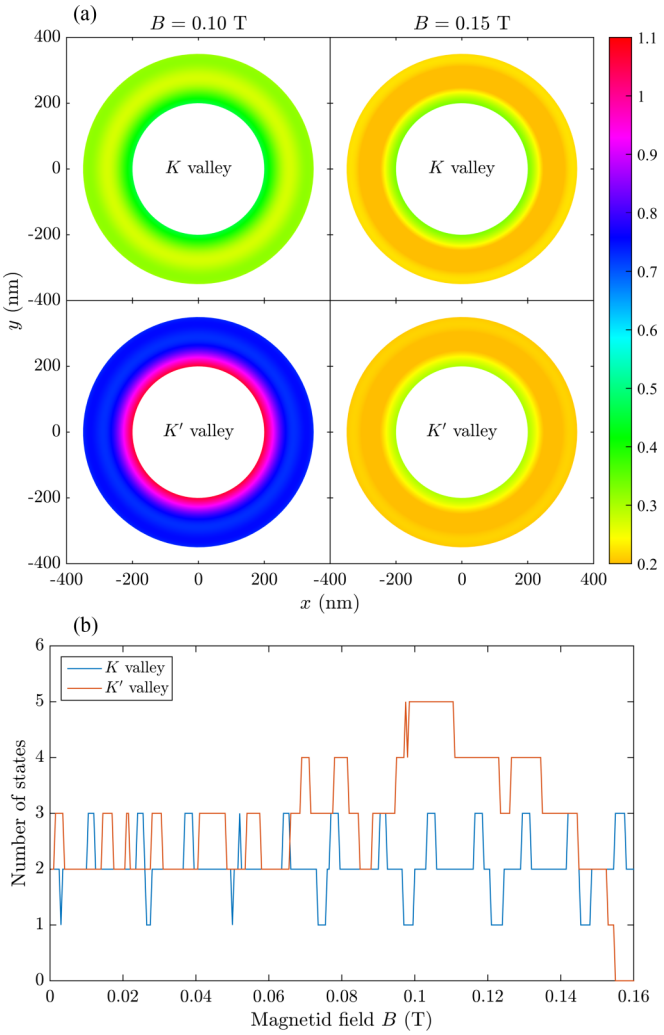

FIG. 9. (a) Valley-resolved local density of states (arbitrary units) for a graphene ring with $R_1 = 200$ nm and $R_2 = 350$ nm. States are sampled in the energy range between -12 and -10 meV indicated by the dotted lines in Fig. 8. The two columns correspond to magnetic fields of 0.1 and 0.15 T, respectively. (b) Valley-resolved number of states in the same energy range.

Fig. 9(b). Thus, at $B = 0.1$ T there are five and two states in the K and K' valley, respectively, whereas at $B = 0.15$ T both valleys contain precisely two states. Furthermore, above $B \approx 0.155$ T, no states with energy between E_1 and E_2 are found in the K' valley, leading to complete valley polarization. The pronounced difference between valleys at certain B fields could potentially be beneficial for applications in valleytronics. We note, however, that complete decoupling of valleys is an idealization resulting from the simple model. In reality, any disorder at the edges or elsewhere will introduce valley mixing. A sufficiently strong magnetic field might suppress valley mixing due to the outer edge by focusing the relevant states in the inner portion of the ring, as shown in Fig. 4.

IV. SUMMARY

In summary, graphene nanorings in magnetic fields have been considered. By applying the Dirac approximation, an

explicit eigenvalue condition valid for arbitrary field strength, geometry, and confining mass term has been derived. The special cases of vanishing inner and outer barriers describe graphene dots and antidots, respectively, and have been investigated separately. The Dirac approach has been validated by comparison with atomistic simulations. Moreover, we have compared the results of the Dirac approach to recent magneto-transport measurements for relatively large graphene rings. The calculated position of Aharonov–Bohm resonances is found to agree well with such experiments. By studying the valley-resolved LDOS we highlight the valleytronics potential of these structures.

ACKNOWLEDGMENTS

The authors gratefully acknowledge the financial support from the Center for Nanostructured Graphene (Project No. DNRF103) financed by the Danish National Research Foundation and from the QUSCOPE project financed by the Villum Foundation.

APPENDIX: GENERAL EIGENSTATES AND EIGENVALUE CONDITION

The full f spinor component for the ring system is determined by Eq. (4), with $\beta = 0$ in region 1 and $\alpha = 0$ in region 2, giving

$$f(r) = Ne^{-\rho^2/2}\rho^{-m}\begin{cases} L^{-m}_{\epsilon^2-\delta^2-\delta_K}(\rho^2), & \rho < \rho_1 \\ \alpha L^{-m}_{\epsilon^2-\delta_K}(\rho^2) + \beta U^{1-m}_{\delta_K-\epsilon^2}(\rho^2), & \rho \in [\rho_1,\rho_2] \\ \gamma U^{1-m}_{\delta_K+\delta^2-\epsilon^2}(\rho^2), & \rho > \rho_2, \end{cases} \tag{A1}$$

where N, α, β, and γ are constants. The constants α, β, and γ are determined by requiring continuity of the wave-function spinors on the boundaries between the different regions and N is determined by the normalization condition $\int(|\psi_A|^2 + |\psi_B|^2)d^2r = 1$. By using Eq. (1), the second spinor component can be expressed as $\psi_B = v_F\Pi_\pm\psi_A/[E + \Delta(\rho)]$. This component thus has the form $\psi_B = i(2\pi)^{-1/2}g(\rho)e^{i(m+1)\phi}$ with radial part

$$g(\rho) = \frac{1}{2(\epsilon + \delta_\rho)}\left(-\frac{d}{d\rho} \pm \frac{m}{\rho} \pm \rho\right)f(\rho). \tag{A2}$$

For the K valley, continuity of f and g then yields the condition

$$g^{(K)}(\rho) = Ne^{-\rho^2/2}\rho^{-m-1}\begin{cases} (\delta-\epsilon)L^{-1-m}_{\epsilon^2-\delta^2}(\rho^2), & \rho < \rho_1 \\ -\epsilon\alpha L^{-m}_{\epsilon^2}(\rho^2) + \frac{\beta}{\epsilon}U^{-m}_{-\epsilon^2}(\rho^2), & \rho \in [\rho_1,\rho_2] \\ \gamma U^{-m}_{\delta^2-\epsilon^2}(\rho^2)/(\delta+\epsilon), & \rho > \rho_2. \end{cases} \tag{A3}$$

The eigenvalue condition for a finite Δ is determined by requiring continuity of both wave-function spinor components, Eqs. (A1) and (A3), at both the R_1 and R_2 boundaries, which yields

$$\begin{aligned} 0 =& \Big\{\epsilon U^{1-m}_{1-\epsilon^2}(\rho_2^2)\big[\epsilon L^{-m-1}_{\epsilon^2}(\rho_1^2)L^{-m}_{\epsilon^2-\delta^2-1}(\rho_1^2) + (\delta-\epsilon)L^{-m}_{\epsilon^2-1}(\rho_1^2)L^{-m-1}_{\epsilon^2-\delta^2}(\rho_1^2)\big]U^{-m}_{\delta^2-\epsilon^2}(\rho_2^2) \\ &- (\delta+\epsilon)U^{-m}_{-\epsilon^2}(\rho_2^2)\big[\epsilon L^{-m-1}_{\epsilon^2}(\rho_1^2)L^{-m}_{\epsilon^2-\delta^2-1}(\rho_1^2) + (\delta-\epsilon)L^{-m}_{\epsilon^2-1}(\rho_1^2)L^{-m-1}_{\epsilon^2-\delta^2}(\rho_1^2)\big]U^{1-m}_{\delta^2-\epsilon^2+1}(\rho_2^2) \\ &- \big[\epsilon(\delta-\epsilon)U^{1-m}_{1-\epsilon^2}(\rho_1^2)L^{-m-1}_{\epsilon^2-\delta^2}(\rho_1^2) - U^{-m}_{-\epsilon^2}(\rho_1^2)L^{-m}_{\epsilon^2-\delta^2-1}(\rho_1^2)\big] \\ &\times \big[L^{-m}_{\epsilon^2-1}(\rho_2^2)U^{-m}_{\delta^2-\epsilon^2}(\rho_2^2) + \epsilon(\delta+\epsilon)L^{-m-1}_{\epsilon^2}(\rho_2^2)U^{1-m}_{\delta^2-\epsilon^2+1}(\rho_2^2)\big]\Big\} \\ &\times \big\{\big[\epsilon^2 L^{-m-1}_{\epsilon^2}(\rho_1^2)U^{1-m}_{1-\epsilon^2}(\rho_1^2) + L^{-m}_{\epsilon^2-1}(\rho_1^2)U^{-m}_{-\epsilon^2}(\rho_1^2)\big]U^{-m}_{\delta^2-\epsilon^2}(\rho_2^2)\big\}^{-1}. \end{aligned} \tag{A4}$$

The spinor components in the special case of the infinite-mass term are obtained from Eq. (4) by using the approximations (5) and (6) in regions 1 and 3 and expanding prefactors around $\delta \to \infty$, keeping dominant terms, which for the f spinor in the K valley gives

$$f^{(K)}(\rho) \simeq Ne^{-\rho^2/2}\rho^{-m}\begin{cases} \frac{e^{\frac{1}{2}\rho(4\delta+\rho)}\delta^{-m}(-\rho)^m}{2\sqrt{\pi}\sqrt{\delta\rho}}, & \rho < \rho_1 \\ \alpha U^{1-m}_{1-\epsilon^2}(\rho^2) + \beta L^{-m}_{\epsilon^2-1}(\rho^2), & \rho \in [\rho_1,\rho_2] \\ \gamma\frac{\sqrt{\pi}e^{\frac{1}{2}\rho(\rho-4\delta)}(\delta\rho)^{m-\frac{1}{2}}}{\Gamma(\delta^2)}, & \rho > \rho_2. \end{cases} \tag{A5}$$

The second spinor component is determined by Eq. (A2), which in the K valley yields

$$g^{(K)}(\rho) \simeq Ne^{-\rho^2/2}\rho^{-1-m}\begin{cases} -\frac{\rho e^{\frac{1}{2}\rho(4\delta+\rho)}\delta^{-m}(-\rho)^m}{2\sqrt{\pi}\sqrt{\delta\rho}}, & \rho < \rho_1 \\ -\epsilon\alpha L^{-m-1}_{\epsilon^2}(\rho^2) + \frac{\beta}{\epsilon}U^{-m}_{-\epsilon^2}(\rho^2), & \rho \in [\rho_1,\rho_2] \\ \gamma\frac{\sqrt{\pi}\rho e^{\frac{1}{2}\rho(\rho-4\delta)}(\delta\rho)^{m-\frac{1}{2}}}{\Gamma(\delta^2)}, & \rho > \rho_2. \end{cases} \tag{A6}$$

For an infinite-mass term, an equivalent boundary condition is requiring zero outward particle current on the boundaries of the ring. This leads to the condition [36] $\psi_A = -ie^{-i\theta}\psi_B$, where θ is the angle of the normal vector pointing away from the boundary with $\theta = \phi$ on the outer boundary and $\theta = \phi + \pi$ on the inner boundary. This is equivalent to $f(R_1) = -g(R_1)$ and $f(R_2) = g(R_2)$. It is worth noting that applying this boundary condition gives rise to the same eigenvalue condition as taking the limit of $\Delta \to \infty$, as given by Eq. (7). In fact, the spinors, Eqs. (A5) and (A6), show directly that $f/g = -1$ for all $\rho < \rho_1$ and $f/g = 1$ for all $\rho > \rho_2$, thus proving that the boundary conditions are compatible. The advantage of using Δ in the derivation is that it becomes straightforward to include the case of a finite Δ, which could be useful for systems with soft confinement. It also allows us to verify that the $\Delta \to \infty$ limit is well defined by comparing it to calculations with varying values of Δ.

[1] K. S. Novoselov, A. K. Geim, S. Morozov, D. Jiang, M. Katsnelson, I. Grigorieva, S. Dubonos, and A. Firsov, Nature (London) **438**, 197 (2005).

[2] A. H. C. Neto, F. Guinea, N. M. R. Peres, K. S. Novoselov, and A. K. Geim, Rev. Mod. Phys. **81**, 109 (2009).

[3] L. Yang, C.-H. Park, Y.-W. Son, M. L. Cohen, and S. G. Louie, Phys. Rev. Lett. **99**, 186801 (2007).

[4] B. Obradovic, R. Kotlyar, F. Heinz, P. Matagne, T. Rakshit, M. D. Giles, M. A. Stettler, and D. E. Nikonov, Appl. Phys. Lett. **88**, 142102 (2006).

[5] Y.-W. Son, M. L. Cohen, and S. G. Louie, Phys. Rev. Lett. **97**, 216803 (2006).

[6] L. A. Ponomarenko, F. Schedin, M. I. Katsnelson, R. Yang, E. W. Hill, K. S. Novoselov, and A. K. Geim, Science **320**, 356 (2008).

[7] S. Schnez, F. Molitor, C. Stampfer, J. Güttinger, I. Shorubalko, T. Ihn, and K. Ensslin, Appl. Phys. Lett. **94**, 012107 (2009).

[8] S. Russo, J. B. Oostinga, D. Wehenkel, H. B. Heersche, S. S. Sobhani, L. M. K. Vandersypen, and A. F. Morpurgo, Phys. Rev. B **77**, 085413 (2008).

[9] M. Huefner, F. Molitor, A. Jacobsen, A. Pioda, C. Stampfer, K. Ensslin, and T. Ihn, Phys. Status Solidi B **246**, 2756 (2009).

[10] D. Cabosart, A. Felten, N. Reckinger, A. Iordanescu, S. Toussaint, S. Faniel, and B. Hackens, Nano Lett. **17**, 1344 (2017).

[11] T. G. Pedersen, C. Flindt, J. Pedersen, N. A. Mortensen, A.-P. Jauho, and K. Pedersen, Phys. Rev. Lett. **100**, 136804 (2008).

[12] J. A. Fürst, J. G. Pedersen, C. Flindt, N. A. Mortensen, M. Brandbyge, T. G. Pedersen, and A.-P. Jauho, New J. Phys. **11**, 095020 (2009).

[13] M. Kim, N. S. Safron, E. Han, M. S. Arnold, and P. Gopalan, Nano Lett. **10**, 1125 (2010).

[14] J. Eroms and D. Weiss, New J. Phys. **11**, 095021 (2009).

[15] Q. Xu, M.-Y. Wu, G. F. Schneider, L. Houben, S. K. Malladi, C. Dekker, E. Yucelen, R. E. Dunin-Borkowski, and H. W. Zandbergen, ACS Nano **7**, 1566 (2013).

[16] A. J. M. Giesbers, E. C. Peters, M. Burghard, and K. Kern, Phys. Rev. B **86**, 045445 (2012).

[17] J. V. Gomes and N. M. R. Peres, J. Phys.: Condens. Matter **20**, 325221 (2008).

[18] S. J. Brun, M. R. Thomsen, and T. G. Pedersen, J. Phys.: Condens. Matter **26**, 265301 (2014).

[19] M. R. Thomsen, S. J. Brun, and T. G. Pedersen, J. Phys.: Condens. Matter **26**, 335301 (2014).

[20] J. G. Pedersen and T. G. Pedersen, Phys. Rev. B **84**, 115424 (2011).

[21] J. G. Pedersen and T. G. Pedersen, Phys. Rev. B **87**, 235404 (2013).

[22] J. G. Pedersen and T. G. Pedersen, Phys. Rev. B **85**, 035413 (2012).

[23] L. L. Li, M. Zarenia, W. Xu, H. M. Dong, and F. M. Peeters, Phys. Rev. B **95**, 045409 (2017).

[24] S. Schnez, K. Ensslin, M. Sigrist, and T. Ihn, Phys. Rev. B **78**, 195427 (2008).

[25] M. Grujić, M. Zarenia, A. Chaves, M. Tadić, G. A. Farias, and F. M. Peeters, Phys. Rev. B **84**, 205441 (2011).

[26] D. R. da Costa, A. Chaves, M. Zarenia, J. M. Pereira, Jr., G. A. Farias, and F. M. Peeters, Phys. Rev. B **89**, 075418 (2014).

[27] P. Recher, B. Trauzettel, A. Rycerz, Y. M. Blanter, C. W. J. Beenakker, and A. F. Morpurgo, Phys. Rev. B **76**, 235404 (2007).

[28] D. S. L. Abergel, V. M. Apalkov, and T. Chakraborty, Phys. Rev. B **78**, 193405 (2008).

[29] D. A. Lovey, G. Usaj, L. E. F. Foa Torres, and C. A. Balseiro, Phys. Rev. B **93**, 245434 (2016).

[30] R. Balog, B. Jørgensen, L. Nilsson, M. Andersen, E. Rienks, M. Bianchi, M. Fanetti, E. Lægsgaard, A. Baraldi, S. Lizzit, Z. Sljivancanin, F. Besenbacher, B. Hammer, T. G. Pedersen, P. Hofmann, and L. Hornekær, Nat. Mater. **9**, 315 (2010).

[31] S. Bhowmick, A. K. Singh, and B. I. Yakobson, J. Phys. Chem. C **115**, 9889 (2011).

[32] I. S. Gradshteyn and I. M. Ryzhik, *Table of Integrals, Series, and Products*, 5th ed. (Academic Press, London, 1994).

[33] N. M. Temme, SIAM J. Math. Anal. **21**, 241 (1990).

[34] D. A. Bahamon, A. L. C. Pereira, and P. A. Schulz, Phys. Rev. B **79**, 125414 (2009).

[35] M. Fujita, K. Wakabayashi, K. Nakada, and K. Kusakabe, J. Phys. Soc. Jpn. **65**, 1920 (1996).

[36] M. V. Berry and R. J. Mondragon, Proc. R. Soc. London, Ser. A **412**, 53 (1987).